

Integrated optical multi-ion quantum logic

Karan K. Mehta,* Chi Zhang, Maciej Malinowski, Thanh-Long Nguyen, Martin Stadler, and Jonathan P. Home
Department of Physics & Institute for Quantum Electronics, ETH Zürich, Switzerland
 (Dated: June 24, 2022)

Practical and useful quantum information processing (QIP) requires significant improvements with respect to current systems, both in the error rates of basic operations and in scale. Individual trapped-ion¹ qubits' fundamental qualities are promising for long-term systems², but the optics involved in their precise control are a barrier to scaling³. Integration of optics into ion traps can make such systems simultaneously more robust and parallelizable, as suggested by previous work with single ions⁴. Here we use scalable planar-fabricated optics to achieve high-fidelity multi-ion quantum logic gates, often the limiting elements in building up the precise, large-scale entanglement essential to quantum computation. Light is efficiently delivered to a trap chip in a cryogenic environment via direct fiber coupling on multiple channels, eliminating the need for beam alignment into vacuum systems and cryostats and lending robustness to vibrations and beam pointing drifts. This allows us to perform ground-state laser cooling of ion motion, and implement gates generating two-ion entangled states with fidelities $> 99.3(2)\%$. This work demonstrates hardware that reduces noise and drifts in sensitive quantum logic, and simultaneously offers a route to practical parallelization for high-fidelity quantum processors⁵. Similar devices may also find applications in neutral atom and ion-based quantum-sensing and timekeeping⁶.

Scaling quantum computing systems while continuing to improve operation fidelities over current systems is the central practical challenge in achieving general, large-scale quantum computation and simulation. Trapped-ion qubits' long coherence times and high-fidelity gates⁷⁻⁹ are likely to be valuable in managing overheads associated with quantum error correction¹⁰, while their fundamental indistinguishability may assist in minimizing control system complexity as systems grow. However, the bulk optics arranged over meters-long free-space paths typically used for trapped-ion control are a major source of drift and noise, and are furthermore challenging to parallelize, particularly in 2D trap geometries¹¹.

Previous work has demonstrated that planar-fabricated nanophotonic waveguides integrated with surface-electrode ion traps offer advantages over free-space approaches in beam pointing and phase stability, power usage, addressability, and parallelizability⁴. The free-space input coupling and low efficiencies in the early work (33 dB loss from input to ion) compromised the potential advantages in stability and limited the utility

of the delivered light for motional coupling, which is essential for both ground-state cooling of ion motion and multi-qubit quantum logic.

In this Letter, we use integrated optics to drive multi-ion entangling quantum logic with fidelities competitive with those in state-of-the-art experiments across qubit platforms. Our experiments leverage efficient interfacing of multiple input fibers to integrated waveguides in a cryogenic ion trap chip (~ 2 dB losses at $\lambda = 729$ nm) via direct attachment. We characterize limiting noise sources, finding significant room for future improvements in this context. The scalability and precision simultaneously afforded with this approach is promising for pursuit of large-scale computation and simulation, and we anticipate similar techniques will find broad application across a range of atom-based technologies.

We designed trap devices with integrated photonics¹³ for fabrication in an openly accessible commercial foundry¹⁴. An optical micrograph of the device studied in this work is shown in Fig. 1. A surface-electrode Paul trap¹⁵ is formed in the top gold layer of a microfabricated chip, and designed to confine $^{40}\text{Ca}^+$ ions $50\ \mu\text{m}$ above the surface at the three zones labeled in Fig. 1b. The trapping potential is formed by radiofrequency (RF)

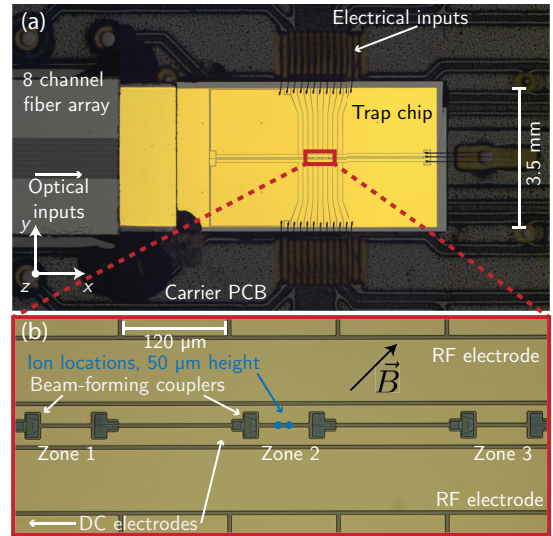


FIG. 1: (a) Optical micrograph of the assembled ion trap device with 8-channel fiber array attached; optical fibers extend from the device to a vacuum feedthrough, with optical inputs via standard connectors outside the vacuum chamber. (b) Zoom-in near the trap zones, showing electrode openings for light from waveguide couplers at the three trap zones (zone 3 was used in the experiments below).

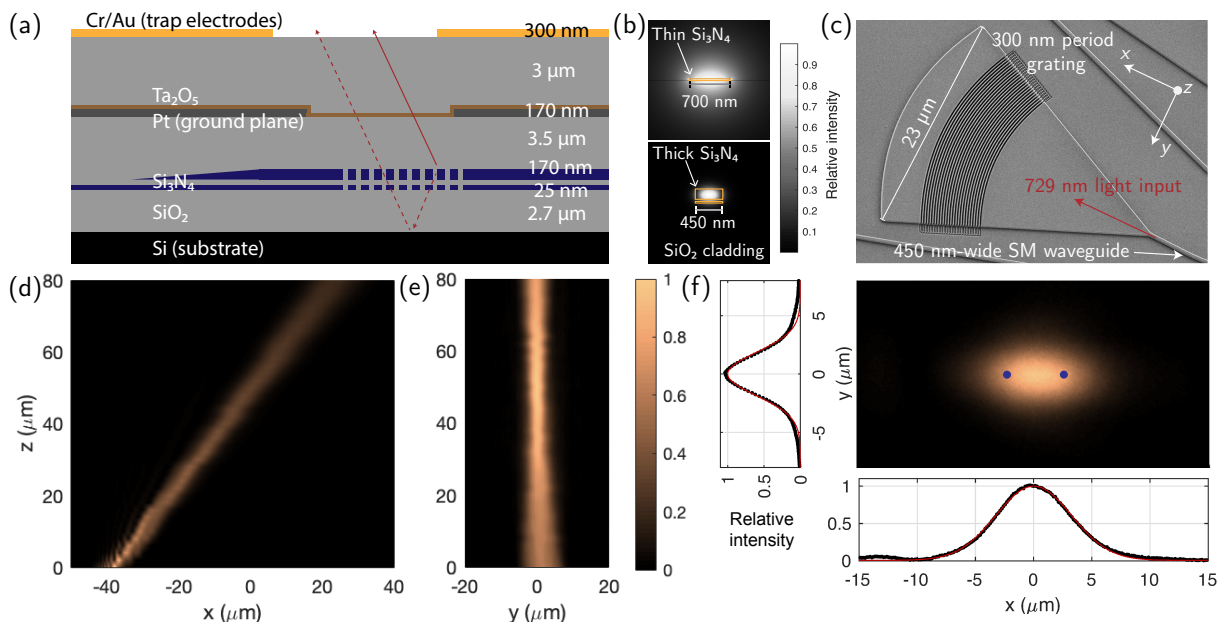


FIG. 2: (a) Layer stackup in trap fabrication. The top gold layer forms the electrodes for the Paul trap, to which RF and DC potentials are applied to confine ions $50 \mu\text{m}$ above the surface. The lower platinum serves as a ground plane, and waveguides/gratings are formed in the SiN. The Si substrate is additionally used as a bottom reflector to increase the grating efficiency¹². (b) Simulated intensity profiles of quasi-TE modes (\vec{E} polarized predominantly along the horizontal) of the two waveguide cross-sections, with core areas outlined in gold. (c) Scanning-electron-microscope image of a fabricated grating, showing photolithographically defined gratings/tapers, and e-beam written grating lines with 300 nm period. (d) and (e) 729 nm-beam emission profiles in the xz and yz planes, obtained from image stacks of radiated field at various heights z above the trap electrode layer. (f) Intensity pattern at the the trap height $z = 50 \mu\text{m}$; radiation is polarized predominantly along \hat{y} , and Gaussian fits indicate $1/e^2$ waist radii in the xy plane of $w_x = 6.5 \mu\text{m}$ and $w_y = 3.7 \mu\text{m}$. Blue dots label trapped ion positions in the radiated beam and confining potential applied in experiments below.

and DC potentials applied to the electrodes. Light controlling the ions is input to the device via an attached multi-channel fiber V-groove array.

Fig. 2a shows the layers comprising the device. A platinum layer forms a ground plane beneath the trap electrodes, to avoid loss and photocarrier-induced modulation of the RF that may result from RF fields exposed to the silicon, as well as to shield ions from charges in the substrate¹⁶. Between this ground plane layer and the substrate, thin-film silicon nitride (SiN) is patterned to form waveguides and gratings, with structures implemented for wavelengths used for coherent qubit control (729 nm) and repumping (854 and 866 nm wavelengths¹⁷).

A thin 25 nm-thick SiN layer supports a weakly-confined optical mode with mode area matched to a standard single-mode fiber at these wavelengths (Fig. 2b); these waveguides extend to the chip edge to interface to input/output optical fibers. To route light on chip, power in this mode is coupled to a highly-confined mode in a thicker core (consisting of an additional 170 nm-thick layer above) via an adiabatic taper over lengths of $\sim 1 \text{ mm}$ ¹⁴. These structures allow coupling from multiple attached fibers to on-chip waveguides with measured insertion losses of 1.4 dB (see Methods), obviating precise beam alignment and allowing optical delivery to ions

in our cryostat through simple fiber feedthroughs on the outer vacuum chamber. This beam delivery also suppresses noise from beam-pointing fluctuations or cryostat vibrations.

Input light is routed to the trap zones shown in Fig. 1b, where a waveguide taper expands the lateral mode diameter and a series of curved grating lines serve to emit light into a designed beam. Openings in the trap electrodes transmit the light and are included symmetrically around each trap zone. These windows in our designs are exclusively in the center DC electrodes, and simulations indicate a negligible impact on the RF pseudopotential.

Gratings (Fig. 2c) for 729 nm light are designed to uniformly illuminate two ions oriented along the trap axis \hat{x} , and hence focus along \hat{y} and emit a roughly collimated beam along \hat{x} . Grating emission is characterized by scanning the focal plane of a high-NA microscope up from the chip surface and capturing a stack of images of the emitted intensity profile at various heights^{4,12} (see Methods). Cross-sectional profiles, and the beam profile at the ion trap height of $z = 50 \mu\text{m}$ measured with this method are shown in Fig. 2c-e.

After the trap die is wirebonded to a carrier PCB and the fiber array is attached, the resulting assembly is mounted in a cryogenic vacuum apparatus and cooled to $\sim 7 \text{ K}$ for ion trap experiments. The fiber array is at-

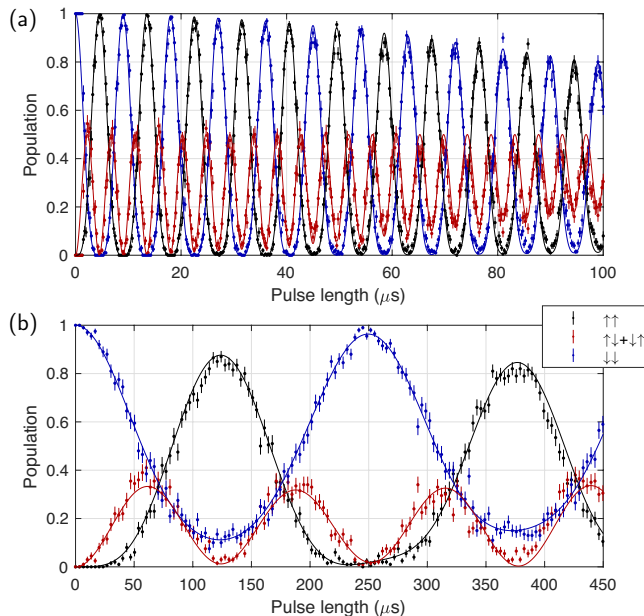


FIG. 3: (a) Coherent manipulation of two ions with laser frequency resonant with the carrier transition at ω_0 . Fits to theory (solid lines) indicate Rabi frequency imbalance between the two ions $< 1 \times 10^{-2}$. (b) Population evolutions upon application of a pulse resonant with the blue sideband ($\omega = \omega_0 + \omega_{\text{STR}}$) on the stretch mode, after sideband cooling with light coupled via the integrated couplers. Lines correspond to theoretical evolutions with $\bar{n}_{\text{STR}} = 0.05$.

tached in a fashion that allows us to maintain low fiber-chip coupling losses (~ 2 dB) on each channel despite the temperature drop from 300 K (see Methods).

Light emitted by the 729 nm couplers drives transitions on all pairs of transitions between the $4S_{\frac{1}{2}}$ and $3D_{\frac{5}{2}}$ manifolds with $|\Delta m_J| \leq 2$ due to the lack of any symmetry between the propagation or polarization vectors of the radiation and the magnetic field of ~ 6 G along $\hat{x} + \hat{y}$, which defines the quantization axis (indicated in Fig. 1b). For experiments below, we choose qubit states $|\downarrow\rangle = |4S_{\frac{1}{2}}, m_J = -\frac{1}{2}\rangle$ and $|\uparrow\rangle = |3D_{\frac{5}{2}}, m_J = -\frac{1}{2}\rangle$, owing to the relatively low differential Zeeman shift (and hence minimal sensitivity to magnetic field fluctuations) of the corresponding transition (0.56 MHz/G).

In our experiments, two ions are confined in a potential well with axial center-of-mass (COM) mode frequency $\omega_{\text{COM}} = 2\pi \times 1.2$ MHz (along \hat{x}), with a resulting ion spacing of $5 \mu\text{m}$. Radial mode frequencies are between 3.7 and 5.7 MHz. In each experimental shot, all motional modes are Doppler cooled, and axial motion is further cooled with electromagnetically-induced-transparency (EIT) cooling¹⁸. This leaves axial modes with mean phonon numbers $\bar{n} \approx 0.5$, and radial modes with $\bar{n} \approx 5 - 15$. The qubit is prepared in the $|\downarrow\rangle$ state via frequency-selective optical pumping on the quadrupole transition with infidelities $< 10^{-4}$ (see Methods).

Coherent single-qubit rotations on two ions resulting

from a 729 nm pulse resonant with the qubit transition following state preparation and cooling are shown in Fig. 3a. Observed Rabi frequencies are consistent with expectation¹⁹, given this beam profile, power, and total loss (6.4 dB input-to-ion, see Methods). DC potentials are applied to translate ions along \hat{x} to positions of equal intensity in the beam (Fig. 2f). The observed Rabi oscillations allow us to bound the Rabi frequency imbalance ($|1 - \Omega_1/\Omega_2|$) seen by the two ions to $< 1 \times 10^{-2}$. This balancing is sensitive to ion positioning at the level of ~ 100 nm; despite the exposed dielectric on the trap surface due to the grating windows and gaps between electrodes, we observe that this positioning is stable over hours of experimenting with two-ion chains. The decay in Rabi oscillation amplitude is consistent with that expected given the thermal occupancy of the Doppler-cooled radial modes²⁰.

Ramsey measurements on single ions were performed to assess qubit coherence. With the integrated 729 nm beam path, we observe T_2^* contrast decay times (see Fig. 7 and Methods) significantly longer than observed using the same light addressing the ion through a free-space path. These decays are dominated by phase noise in our 729 nm light, and we attribute the enhancement in coherence to the fact that cryostat vibrations relative to the optical table result in phase fluctuation at the ion in the free-space configuration, which is suppressed for the integrated beam path due to the common motion of the grating and trap.

Multi-ion quantum logic is mediated by shared motional modes; high-fidelity implementations require near-ground-state cooling, particularly of the modes used to enact the gates. We implement gates using axial modes of motion, and choose the mode in which ions oscillate out of phase (which we refer to as the “stretch” mode, at $\omega_{\text{STR}} = \sqrt{3}\omega_{\text{COM}}$) since the opposite phases of oscillation for the two ions renders this mode relatively insensitive to electric-field noise that heats ion motion²¹. We use the light delivered by the integrated couplers to implement pulsed sideband cooling²⁰. Blue sideband flopping following ground-state cooling (Fig. 3b) indicates a mean phonon number $\bar{n}_{\text{STR}} \approx 0.05$.

We proceed to implement entangling operations mediated by the ground-state-cooled stretch mode. Mølmer-Sørensen gates²² apply the unitary $\hat{U}_{\text{MS}}(\phi) = \exp[-i\pi(\sum_k \hat{\sigma}_{\phi,k})^2/8]$, with $\hat{\sigma}_{\phi,k} = \cos(\phi)\hat{\sigma}_{x,k} + \sin(\phi)\hat{\sigma}_{y,k}$ representing Pauli operators on qubit k (with $|\uparrow\rangle$ and $|\downarrow\rangle$ the eigenstates of $\hat{\sigma}_z$). ϕ is set by laser phases. We implement \hat{U}_{MS} by applying two tones detuned from the stretch mode sidebands of the 729 nm carrier transition at $\omega_{\pm} = \omega_0 \pm (\omega_{\text{STR}} + \delta)$ (see Fig. 4). Starting from $|\downarrow\downarrow\rangle$, the ideal implementation generates the Bell state $\frac{1}{\sqrt{2}}(|\downarrow\downarrow\rangle - i|\uparrow\uparrow\rangle)$ after a pulse time $\tau_g = 2\pi/\delta$. Measured population evolutions as a function of pulse duration are shown in Fig. 4b, together with theoretical predictions for an ideal gate. To measure the coherence of the state produced at $\tau_g = 66 \mu\text{s}$, we apply identical single qubit rotations $\hat{R}(\theta, \phi_a) = \exp(-i\theta\hat{\sigma}_{\phi_a}/2)$

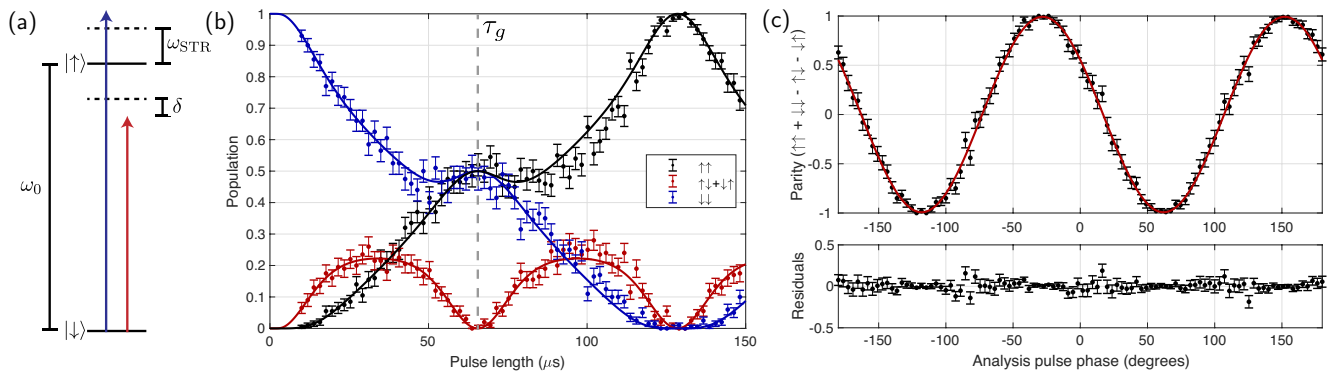


FIG. 4: Integrated implementation of a 2-ion quantum logic gate. (a) Optical frequencies applied to drive a Mølmer-Sørensen gate; in our experiments $\omega_0 = 2\pi \times 411$ THz (729 nm), $\omega_{\text{STR}} = 2\pi \times 2.0$ MHz, and the detuning from motional sidebands is $\delta = 2\pi \times 15$ kHz. (b) Population evolutions as a function of pulse duration; solid lines show ideal gate evolutions from theory, with gate time as the only free parameter. (c) Parity oscillations observed upon scanning the phase of an “analysis” $\pi/2$ pulse after the gate time $\tau_g = 66 \mu\text{s}$. The fit contrast (red line) of 0.992(2), together with the even populations measured at the gate time 0.994(1), indicate a Bell state generated with fidelity 0.993(2). In both (b) and (c), each point represents an average over 200 experimental shots, with error-bars indicating 1σ standard errors from projection noise.

to both ions with $\theta = \pi/2$ after the gate, with variable phase ϕ_a . These “analysis” pulses map individual qubit states to superpositions on the equator of the Bloch sphere, and the entangled Bell state to states of varying parity depending on $\phi_a - \phi$; here, parity is defined as $\mathcal{P} = P_{\uparrow\uparrow} + P_{\downarrow\downarrow} - P_{\uparrow\downarrow} - P_{\downarrow\uparrow}$, where P s are the populations measured in the four possible two-ion outcomes. The contrast of the parity oscillations as a function of ϕ_a is a direct measure of the coherence of the Bell-state generated at τ_g ²³. A maximum-likelihood fit to the data indicates a contrast of 99.2(2)%, together with the populations measured at the gate time (99.4(1)%) indicating a total Bell-state fidelity of 99.3(2)%, including state preparation and measurement error.

Contributing error sources are summarized in Table I, with leading infidelities arising from motional heating and mode frequency drifts, and laser frequency noise. We discuss these and improvements possible below, with details presented in the Methods.

We measure a heating rate of $\dot{n} = 60(30)$ quanta/s on the 2.2 MHz stretch mode, resulting in infidelities for the 66 μs gate of 0.2(1)%. This noise can be greatly suppressed in surface traps with similar geometries; we measure heating rates for single-ion axial oscillations at 1.2 MHz to be ~ 3000 quanta/s, indicating E -field noise $\sim 100\times$ higher than other cryogenic surface-electrode traps with similar ion-electrode distance²⁴.

During gate operations, we observe slow drifts of order 100 Hz in the stretch mode frequency. We observe motional frequency deviations correlated to MS-gate light (1.5 mW of 729 nm light propagating to the ions) being switched on and which relax over ~ 10 s-timescales, suggesting photo-induced charging of the unshielded SiO_2 dielectric at the grating windows. Steps taken to minimize this effect, as well as those due to the silicon substrate (also partially exposed to the ion near the gratings) are detailed in the Methods. Our experiments serve as a

baseline as to performance achievable with no shielding of the exposed dielectric; a transparent conductive layer of e.g. indium tin oxide (ITO)²⁵, may significantly reduce these drifts. Although we have implemented the simplest-possible single-loop gate here, multi-loop and composite gate schemes can further suppress errors from such variations²⁶.

Finally, errors from laser noise are inferred from Ramsey measurements (Fig. 7). These could be reduced using improved implementation of acoustic noise cancellation on optical fiber in our system²⁷, together with technical improvements to our laser frequency stabilization.

The only error source fundamental to this choice of qubit is spontaneous emission from the $D_{5/2}$ level, which given its 1.1s lifetime contributes an error of 3×10^{-5} for the initial state and 66 μs gate time employed here (this error scales with τ_g).

The fidelities achieved in this work are within a factor of about 5 of the best demonstrated with trapped

Error source	Infidelity ($\times 10^{-3}$)
Motional mode heating	2(1)
Motional frequency drifts	1
Laser frequency noise	1
Two-ion readout error	0.5
Kerr cross-coupling	0.4
Spectator mode occupancies	0.3
Spontaneous emission	0.03
Total	$\sim 5 \times 10^{-3}$

TABLE I: Error sources and estimated contributions to infidelity of two-qubit Bell state generated here; systematic miscalibration is not included, and expected to contribute also at the 1×10^{-3} level.

ions^{8,9}. While microwave-based schemes are promising for achieving the highest possible fidelities²⁸, we note that the mW-level optical powers in our work are 2-3 orders of magnitude lower than the powers required in microwave gate implementations in planar traps to date^{29,30}, in which gate rates were additionally an order of magnitude lower. Power requirements are likely to be important in determining practicality of larger-scale systems where dissipation is a concern. The much shorter wavelength of optical radiation also allows focusing and straightforward addressing of radiation to particular ions in chains³¹ or in separate trap zones¹², without active cancellation. We measure crosstalk of -60 dB in relative intensity in neighboring zones (see Methods). On the other hand, requirements on long-term laser phase stability and spontaneous emission errors may eventually prove problematic in algorithms with optical gates as gate fidelities progress to the 10^{-5} level; we discuss a route to ameliorating these requirements in ions like $^{40}\text{Ca}^+$ by utilizing both the Zeeman and optical qubit transitions in the Methods.

This work motivates developments along multiple fronts. The wavelengths which can be guided in the current chip should allow laser cooling and readout to be implemented using IR and high intensity visible light³², while materials and waveguides for blue/UV light³³ will allow photoionization, laser cooling, and readout at low optical powers²⁵. This would enable practical, parallel operation of multiple zones with fully integrated beam delivery, in a fashion also extensible to dual-species systems and 2D trap architectures. Implementation of transport between zones in such an architecture would be a natural step towards large-scale computations^{5,34}. Combination of optics for photoionization and incoherent operations with appropriate microwave electrodes could facilitate scaling approaches using microwave coherent manipulation²⁸⁻³⁰. The demonstrated precision of ion positioning here also indicates the practicality of schemes taking advantage of integrated optics' ability to generate spatially structured fields, e.g.¹³, while the high-efficiency fiber-to-chip coupling in cryostats demonstrated here, as well as stable tight focusing enabled by such approaches¹² make possible practical, power-efficient fast gates³⁵.

Beyond their broad relevance in trapped-ion QIP, these approaches may also benefit atomic clocks, whether in portable systems or in precise clocks utilizing multiple trap zones⁶. The techniques developed and demonstrated here are applicable to neutral atom quantum systems as well³⁶.

Appendix: Methods Summary

1. Device design and fabrication

Devices were designed similarly to previous work¹². The grating designs exploit the reflection from the silicon substrate below to increase efficiency per unit length;

a compromise between grating length and efficiency resulted in a designed radiation efficiency of 50% in these devices (defined as upwards-radiated power as a fraction of input power). Emission into a single grating order is ensured by choosing a sufficiently large grating wavenumber $\beta_g = \frac{2\pi}{\Lambda}$ (with Λ the grating period). The curvature of the grating lines is calculated to induce focusing perpendicular to the trap axis along \hat{y} in Fig. 1b, with designed focusing limited to ~ 3 μm waists to relax sensitivity to misalignments in fabrication. Λ is constant over the grating length in these devices to generate an approximately collimated beam along the trap axis.

Grating designs were verified with 3D finite-difference-time-domain (FDTD) simulations (Lumerical FDTD solutions), and 3D simulations of the ion trap potentials were performed in COMSOL; designs were drawn in Cadence Virtuoso.

Various trap and optical designs were drawn on a 2.2×2.2 cm^2 reticle repeated across a 4-inch wafer (Fig. 5). A design drawing of the trap die used in this work is shown in Fig. 5c, together with a magnified view near one of the trap zones with 729 nm and 854/866 nm waveguides and gratings. The three zones with addressing couplers were included with different offsets between the e-beam and photolithography-defined features, to compensate for the ~ 300 nm relative alignment tolerance in the current fabrication.

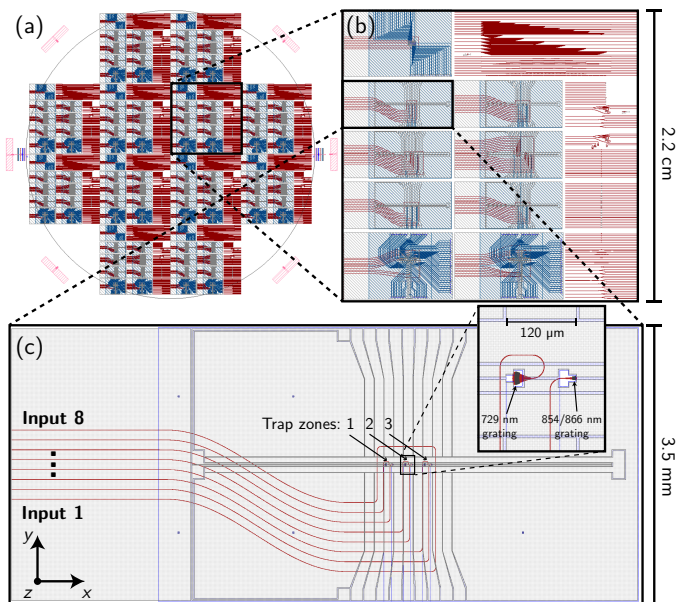


FIG. 5: (a) Mask images for device fabrication across a 4-inch wafer. (b) Individual 2.2×2.2 cm^2 reticle, showing trap designs as well as independent optics test structures. (c) Trap design used in ion experiments presented here. In all images, SiN features are shown in red, the top trap electrode layer in gray, and the ground plane in blue. The 8 waveguides coupled to the fiber array are labeled at the left, with inputs 1 and 8 forming a loop structure used to align the fiber V-groove array.

Fabrication was performed by LioniX International, using TriPleX technology¹⁴. Devices were fabricated on 4-inch silicon wafers with 5-10 Ohm-cm resistivity; the bottom 2.7 μm oxide layer was formed via thermal oxidation, with the waveguide layers formed in LPCVD silicon nitride layers. Following combined stepper photolithography and e-beam patterning of the waveguide/grating features, LPCVD SiO_2 cladding was deposited. The platinum layer was then deposited after planarization, and patterned via contact photolithography ion beam etching; the upper SiO_2 isolation was patterned to allow vias between the two metal layers, after which the upper gold was deposited via sputtering and patterned via contact photolithography and a liftoff procedure to form the trap electrodes.

Diced wafers were delivered to ETH, where die were characterized for optical performance, or else cleaned, packaged and fiber-attached for ion trap experiments.

2. Assembly and fiber attachment

A standard 8-channel fiber V-groove array populated with Nufern S630-HP fibers spaced at 127 μm pitch was purchased from OZ Optics. 8 waveguides extend to the edge of the chip die to interface to the array, with the outer two forming a simple loop structure to be used to align the array by maximizing loop transmission. Standard non-polarization-maintaining fiber is used for simplicity in this work, and in-line fiber polarizers control the input polarization.

Individual trap die were removed from the wafer, and a $1.5 \times 3.5 \text{ mm}^2$ SiO_2 piece of 500 μm thickness was epoxied (EPO-TEK silver epoxy, model H21D) to the top surface of the trap chip at the fiber-coupling edge (Fig. 6, and visible near the fiber array in Fig. 1a). This piece was previously coated in 300 nm Au via electron-beam evaporation on faces exposed to the ion, to minimize possible stray fields. Subsequently the die was coated in a protective photoresist layer and mounted in a custom-machined holder for polishing on standard fiber polishing paper. Polishing reduces roughness and associated loss at the coupling interface, and introduces convex curvature to the facet, important for the fiber attachment as described below. The silicon substrate was scribed with a diamond scribe to break through the native oxide, and after dissolving the protective photoresist, a drop of silver epoxy was applied both to contact the silicon substrate to ground on the carrier PCB, as well as to ensure grounding of the metal on the SiO_2 piece near the fiber array. The trap electrodes were then wirebonded to the contacts on the carrier PCB.

To attach the fiber array, the facet-polished and wire-bonded sample was mounted on a temperature-controlled chuck fixed to a 3-axis tip/tilt/rotation stage and raised to 95°C. The fiber array, held in a custom machined stainless-steel mount in a 3-axis translation stage, was then pressed against the chip in such a fashion that

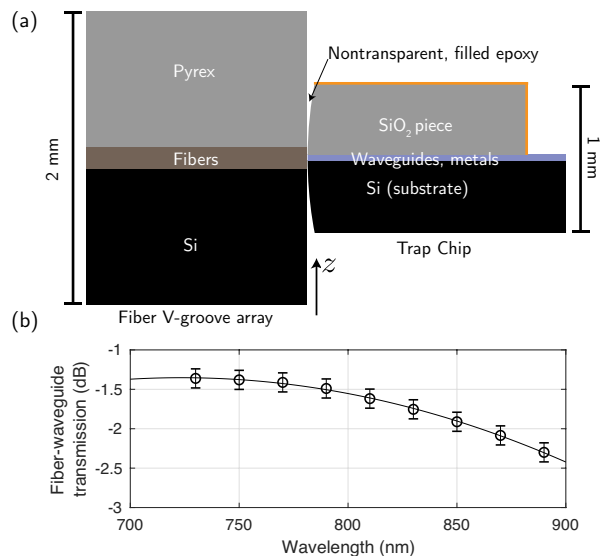


FIG. 6: Fiber attach process and measured single pass fiber-waveguide coupling losses inferred from a loop-back structure on-chip; solid line is a guide to the eye.

static friction between the two interfaces allowed coupling to be passively maintained for hours (see Fig. 6a for a schematic of this interface). Low-temperature curing, non-transparent, filled epoxy (EPO-TEK T7109-19) was then dropped at the two edges and allowed to wick into the gap; this epoxy was chosen as its flexibility should result in robustness to temperature changes. The convex curvature of the trap die at this interface ensures that the epoxy does not interact with the optical mode, allowing choice of mechanically suitable epoxies without restriction to transparent variants, and important to minimize possible photo-effects which can be problematic with adhesives exposed to visible wavelengths. The contact area used for the attachment is therefore about $1 \times 3.5 \text{ mm}^2$. After a few hours at this curing temperature, the assembly was cooled to room temperature, and no drop in transmission was observed. We have performed two attachments in this fashion to date, and found both robust to temperature drops.

The transmission of a single fiber-waveguide interface was measured at various wavelengths within the bandwidth of a CW Ti:sapphire laser, measuring the transmission from input fiber 1 to fiber 8 and subtracting the measured waveguide loss. The broadband nature of this coupling is shown in the measurements in Fig. 6b. Upon applying current to a heater on the carrier PCB near the chip and then cooling the assembly to 7K, we observed a small increase in loss from 1.4 dB to 2.4 dB at 729 nm, but saw no further changes after two additional temperature cycles between room temperature and 7K. These coupling losses compare favorably to previous published work on cryogenic fiber attachment³⁷. This method furthermore allows multiple channels aligned in parallel, and at shorter wavelengths with more demanding alignment

tolerances.

3. Waveguide/grating characterization and optical losses

Structures consisting of waveguides of varying length on chip were included on separate points on the wafer to measure waveguide losses in the high-confinement mode used for routing on chip. These were measured to be 2 dB/cm at 729 nm, and verified with measurements of quality factors of ring resonators also implemented on the wafer. Wavelength-dependent losses were measured from 729 to 920 nm using a tunable CW Ti:sapphire source, with a drop in loss with increasing wavelength suggesting loss due to scattering from sidewall roughness as the dominant source. We hence expect improved lithography can reduce this loss.

Grating emission was profiled (Fig. 2c-e) using a microscope on a vertical translation stage to image the emission at various heights above the chip¹² onto a scientific CCD camera (Lumenera Infinity 3S-1UR), through a 0.95-NA objective (Olympus MPLANAPO50x). An RF modulation input was applied to the current drive of a 730 nm diode laser to reduce the coherence length to avoid reflection artifacts in the imaging system.

With 1.5 mW of 729 nm light input to the fiber outside the cryostat, we observe a 2.6 μ s π -time, which is within 25% of the 2.0 μ s predicted from a first-principles calculation¹⁹ accounting for the measured beam profile, and the total expected loss of 6.4 dB, arising from: 2.4 dB fiber-chip coupling, 1 dB of waveguide loss over the 5 mm path length, and 3 dB grating emission loss. In the π -time calculation we assume the ion sits at the maximum of the 3.7 μ m beam waist along \hat{y} , resulting in a lower-bound given the μ m-scale misalignments in these devices.

In testing power handling of these waveguides, a maximum of 300 mW was coupled into the single-mode waveguides at 729 nm wavelength; we did not observe damage to the waveguides from these intensities. Future work will investigate power handling limits and self-phase modulation in such waveguides at visible wavelengths, relevant to large-scale architectures with power for multiple zones input to a single bus waveguide.

4. Laser/cryogenic apparatus, and trap operation

Diode lasers supply the various wavelengths used in the ion experiments. The 729 nm light used for coherent qubit control is stabilized to a high-finesse reference cavity resulting in a linewidth of order 100 Hz. Light transmitted through the cavity injection-locks a secondary diode, whose output passes through a tapered amplifier (TA) to a free-space double-pass acousto-optic modulator (AOM) setup for switching and frequency tuning, and subsequently a single-pass fiber-coupled AOM

for pulse-shaping. Two tones are applied to this fiber AOM also for generating the two sidebands in the MS gate. In the current experimental path, approximately 9 meters of total length is present before and propagating inside the cryostat that on which acoustic noise is not actively cancelled; vibrations along this length of fiber would contribute to the coherence decay presented below (Fig. 7).

The cryogenic apparatus used for ion trap experiments is similar to that described previously³⁸. Ions are loaded from neutral atom flux from a resistively heated oven within the 4K chamber, followed by two-step photoionization using beams at 423 nm and 389 nm³⁹. Our current fiber feedthrough consists simply of bare 250 μ m-diameter acrylate-coated fibers epoxied (Stycast 2850FT) into a hole drilled in a CF blank flange mounted on the outer vacuum chamber. In the experiments presented in this paper only the 729 nm beam for qubit control was delivered via integrated optics; though waveguide structures for 854 nm/866 nm light were included on chip, these beams were guided together with the shorter wavelengths for convenience given the previously existing optical setup.

DC voltage sets for axial confinement, stray-field compensation, and radial mode rotation were calculated using methods similar to those described in⁴⁰, based on 3D field simulations including the effect of exposed dielectric in our design.

We used these voltage sets to compensate stray fields in 3D by minimizing first and second micromotion sidebands of ion motion using two separate 729 nm beam-paths. Light emitted by the grating has a wavevector $\vec{k}_g = k_{729}(\hat{z} \cos \theta_g + \hat{x} \sin \theta_g)$, where $\theta_g = 37^\circ$ is the emission angle from vertical; this beam hence allows detection of micromotion along \hat{x} and \hat{z} . To compensate with sensitivity along \hat{y} , we used a second beam propagating in free-space along $\vec{k}_f = k_{729}(\hat{x} \cos \theta_f + \hat{y} \sin \theta_f)$ with $\theta_f = 45^\circ$. The calculated compensation voltage sets were used to minimize micromotion (MM) sidebands on both beam paths, which allowed us to achieve first MM sideband to carrier Rabi frequency ratios of $\Omega_{\text{MM}}/\Omega_{\text{car}} \approx 0.01$. We note the requirement for two beams here arises from the typical assumption that the optical field's gradient is nonzero (or, for quadrupole transitions, curvature) only along its propagation direction; this does not hold for transverse focusing to wavelength-scale spots, in which ions undergoing micromotion perpendicular to the beam propagation direction will experience amplitude modulation. Beams focused to wavelength-scale spots may thus allow sensitive compensation along all dimensions using a single beam.

The silicon partially exposed to the ion due to openings in the ground plane near the gratings was a potential concern, as previous work has seen that unshielded semiconductor can be problematic for stable trap operation¹⁶; we note that the substrate was not highly conductive or grounded in that previous work, and the grounding implemented here may be a significant difference. We have

observed charging effects that appear to be related to carrier dynamics in the silicon; in particular, we observe jumps in the motional frequency of order 10 kHz after Doppler cooling and state preparation with the 397 nm beam, which relax on ms-timescales. These jumps were eliminated when a few mW of IR light were input into one of the other waveguide channels on the chip (e.g. input 1). We attribute this to photoexcited carriers in the silicon from light scattered out of the waveguides and gratings, which increase the conductivity of the substrate and more effectively short it to ground, thereby suppressing stray fields originating from the substrate. The gate data shown in this paper was taken with a constant substrate illumination. It is possible that the use of heavily doped silicon would attenuate possible stray fields from the silicon; in a CMOS context, highly-doped and contacted layers at the exposed surfaces could potentially be used for the same purpose.

Additionally, we observed kHz-level drifts in motional frequencies which relaxed on longer timescales of many minutes, which we attribute to charges trapped in or on the surface of the dielectric near the grating windows – this charging was clearly correlated, for example, to the high-power 729 beams used for the MS gate experiments being turned on. To minimize drifts in the motional frequency, we pulsed on the 729 nm beam during the 1 ms-long Doppler cooling pulse applied in each experimental shot, which led to a more constant optical flux through the opening and reduced these drifts to the level of a few 100 Hz; we additionally recalibrate the motional frequency every 15 s during MS gate experiments to minimize the effect of remaining drifts. The extent to which conductive shielding of this exposed dielectric (as recently demonstrated²⁵) reduces the magnitude of these effects will be an interesting question for future experiments.

5. Contributions to Bell-state infidelity and routes to improvement

Here we detail the error sources contributing to the Bell state infidelity achieved via the integrated MS gate (Table I), and discusses routes to improvement.

We measured heating rates on the 2-ion stretch mode at 2.2 MHz used for the MS gates here via fits to sideband flopping following variable wait times, from which we infer heating rates of $\dot{n} = 60(30)$ quanta/s. For the single-loop gates implemented here, this contributes an error $\epsilon_h = \dot{n}\tau_g/2$,⁴¹ resulting in our estimate of $2(1) \times 10^{-3}$.

The motional frequency was recalibrated during the gate experiments every 15 s, and between each recalibration we observed an average drift of 200 Hz magnitude. We used the calibration results to generate a probability density function for the motional frequency error during each experimental shot, which together with simulated infidelity resulting from an error in gate detuning δ resulted in an expectation infidelity of 1×10^{-3} .

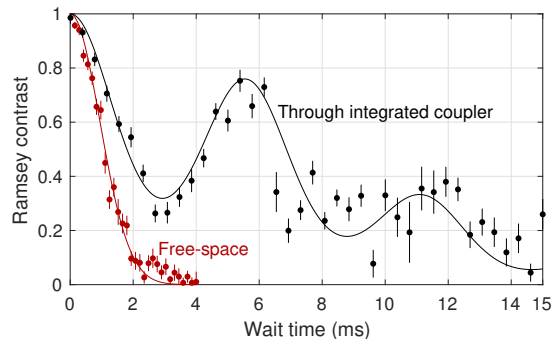


FIG. 7: Ramsey coherence measurements, consisting simply of two $\pi/2$ pulses separated in time by a variable wait time, to assess T_2^* . Data is shown using the same light guided through the in-cryostat fibers and integrated couplers (black points and fit) or through free-space (red points and fit). The fit to the data observed with the integrated coupler was used to infer laser noise parameters relevant to gate infidelity calculation; the observation of significantly faster decoherence when driving with the free-space beam (red points/fit) using the same 729 nm source indicates the integrated beam path’s advantage in insensitivity to cryostat vibrations.

Spin coherence was assessed by means of Ramsey measurements on single qubits. Ramsey decays (Fig. 7) observed when driving the $|S_{\frac{1}{2}}, m_J = -\frac{1}{2}\rangle$ to $|D_{\frac{3}{2}}, m_J = -\frac{1}{2}\rangle$ qubit transition through the integrated gratings were fit by a model with a discrete noise component⁴² corresponding to oscillations in apparent carrier frequency occurring with $2\pi \times 175$ Hz periodicity, with a frequency excursion amplitude of $2\pi \times 160$ Hz, together with a slower Gaussian decay with $1/e$ time of 11 ms. We found consistent decays on the $|S_{\frac{1}{2}}, m_J = -\frac{1}{2}\rangle$ to $|D_{\frac{3}{2}}, m_J = -\frac{3}{2}\rangle$ transition, whose magnetic field sensitivity is $2 \times$ higher, suggesting that laser frequency fluctuations (and not magnetic field drifts) are the dominant contribution. The infidelity resulting from this slow frequency noise was estimated by numerical simulation of the MS gate infidelity resulting from an offset carrier frequency, accounting for the per-shot probability distribution function for the sinusoidal noise inferred from the Ramsey decay; this resulted in an expectation error of 1×10^{-3} .

The use of the stretch mode is advantageous with respect to heating, but introduces sensitivity to radial mode temperatures; variance in occupancy of the “rocking” radial modes can result in varying shifts in the frequency of this mode through a Kerr-type interaction^{43,44} over experimental shots. In our experiments, for technical reasons owing to beam directions required for EIT cooling, radial modes are not ground-state cooled, and after Doppler cooling we observe temperatures corresponding to $\bar{n} \sim 12 - 13$ for the modes at 3.5 MHz and $\bar{n} \sim 5$ for those at 5.5 MHz; these result in an estimate of the resulting infidelity of 4×10^{-4} .

The warm radial modes also contribute to shot-to-shot carrier Rabi frequency fluctuations, since the grat-

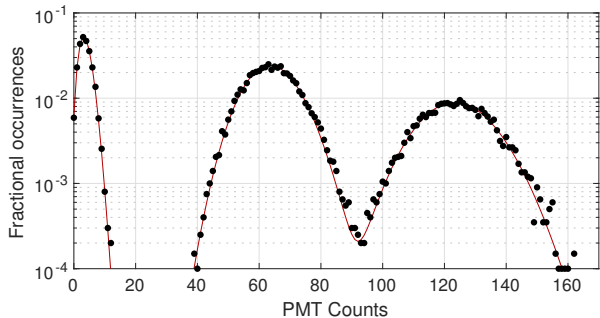


FIG. 8: Histogram of PMT counts observed in detection events over all points in the parity scan of Fig. 4, fitted to a sum of 3 Poissonian distributions. Each distribution corresponds to counts obtained during a $250 \mu\text{s}$ detection period from events with either 0, 1, or 2 ions in the bright state.

ing beam couples to all radial modes (these dominate the decay observed in Rabi oscillations in Figs. 3a and 9a). From the same occupancies given above, we estimate an infidelity of 3×10^{-4} .

Qubit state preparation is based on frequency-selected optical pumping on the quadrupole transition (repeatedly driving a 729 nm π -pulse starting from $|S_{\frac{1}{2}}, m_J = +\frac{1}{2}\rangle$ and repumping with the 854 nm beam to the fast-decaying $P_{\frac{3}{2}}$ levels); we measure preparation of qubits in the starting $|S_{\frac{1}{2}}, m_J = -\frac{1}{2}\rangle$ state with infidelities $< 10^{-4}$. Qubit state detection is based on applying a resonant 397 nm pulse (driving $S_{\frac{1}{2}} \leftrightarrow P_{\frac{1}{2}}$ transitions) for $250 \mu\text{s}$ after each shot and thresholding the number of photon counts detected by our photomultiplier tube (PMT), to infer whether the detection event corresponded to 0, 1, or 2 ions bright. The 1-bright-ion histogram is well separated from the dark distribution and contributes negligible error; however, with the optimal threshold, 0.1% of 1-bright-ion events are mistaken for 2 bright, and vice versa, contributing 0.5×10^{-3} to our Bell-State infidelity.

We implement smooth ramps of RF amplitudes applied to AOMs to generate the gate pulse over times of $\sim 5 \mu\text{s}$, which reduces carrier infidelity from off-resonant driving of the direct drive term in the MS interaction Hamiltonian²² to negligible levels for the current gates.

The effects summarized above together account for about 0.5% infidelity, and we expect systematic offsets resulting from our current calibration approach to additionally enter at the 0.1% level. The gate fidelity could clearly be improved with multiple technical improvements; heating error can be suppressed by $100\times$ if improved trap materials or technical noise sources can allow heating rates comparable to the lowest-noise cryogenic surface traps²⁴. Shielding of the exposed dielectric should reduce motional frequency drifts, and optimal strategies for this are likely to be essential especially for integrated trap chips delivering significant powers in the blue/UV as well. Improved laser coherence is straightforwardly approachable, and ground-state cooling of radial

modes can suppress Kerr cross-coupling and Rabi frequency fluctuations from radial mode occupancies, both of which contribute error roughly quadratic in \bar{n} , by $> 100\times$. Couplers and beam/field geometries in future chips for EIT ground-state cooling of all modes⁴⁵ will be an enabling development. Our current experiments show no obvious limit to fidelity arising from optical integration, which we expect to be capable of approaching the $\sim 10^{-5}$ limit imposed by spontaneous emission using this qubit.

6. Crosstalk between trap zones

Optical radiation brings advantages in the possibility for tight beam focuses addressing individual ions or ensembles within a larger systems.

We quantified crosstalk levels expected in parallel operation of multiple zones in the present device by inputting light to adjacent fiber couplers and measuring the effect on the ion in the experimental trap zone 3 (zones and waveguide inputs labeled in Fig. 5c). Fig. 9a shows single-ion Rabi flopping driven when light is coupled in to input 3, which couples to the 729 nm grating in zone 3. If an ion was being addressed in zone 2 instead, light would be coupled to input 5; when we send the same optical power to input 5, we observe Rabi flopping $1000\times$ slower in zone 3 (Fig. 9b), indicating a relative intensity in this non-addressed zone of -60 dB .

This level of crosstalk appears to arise from a combination of coupling between the waveguides on-chip (i.e. coupling from the waveguide of input 5 to input 3, and then emission by the grating in zone 3), and weak side-

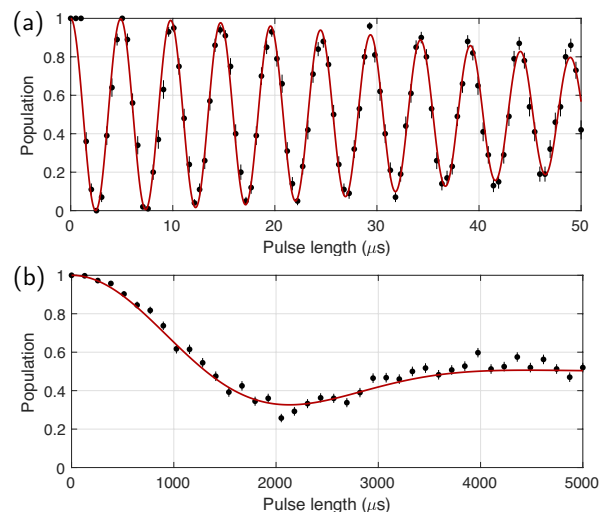


FIG. 9: Rabi flopping (a) at zone 3 with light input through input 3 addressing this zone and (b) in the same zone but with light input through input 5 addressing the neighboring zone. Fits to Rabi oscillations with a Gaussian envelope decay indicate π -times of $2.4 \mu\text{s}$ (a) and 2.6 ms (b).

lobes of emission from the zone 2 grating to the ion in zone 3. Similar levels of crosstalk at -60 dB are observable when feeding in light to input 1, which propagates in a loop around the device and to no grating; the beam profile emitted is also observed to be consistent with that emitted by the 729 nm coupler in zone 3, so we attribute this to coupling between the waveguides fed by input 1 and 3. When polarization is adjusted to minimize transmission to the loop output, the crosstalk drops by 20 dB, suggesting that the bulk of crosstalk into the zone 3 coupler comes from inter-waveguide coupling rather than diffuse scatter at the fiber-chip interface. We expect lower-loss waveguides with less sidewall scattering to reduce this effect. With regards to crosstalk from the emission of the grating itself, this is particularly pronounced in these designs along the axial direction we probe here¹², and we expect optimized arrangements and designs to reduce this source as well. A variety of composite pulse schemes can reduce the impact of coherent errors resulting from residual intensity in quantum algorithms.

7. Hybrid Zeeman/optical qubit encoding

Long sequences of gates conducted using the optical qubit addressed in this work would require phase stability of the driving 729 nm light over the entire algorithm, a challenging technical requirement for algorithms extending beyond many seconds.

We note that the problem with long-term laser phase stability may be ameliorated by hybrid approaches where, for example in $^{40}\text{Ca}^+$, qubits can be stored in the two $S_{\frac{1}{2}}$ Zeeman sublevels (and single-qubit gates implemented via RF magnetic fields), with excitation from one sublevel to the $D_{\frac{5}{2}}$ state only to implement two-qubit interactions.

For each ion, denote the three levels involved $|0\rangle = |S_{\frac{1}{2}}, m_J = -\frac{1}{2}\rangle$, $|1\rangle = |S_{\frac{1}{2}}, m_J = +\frac{1}{2}\rangle$, and $|2\rangle$ a sublevel of the $D_{\frac{5}{2}}$ manifold; $|0\rangle$ and $|1\rangle$ represent the long-term “memory” qubit. $|1\rangle$ is mapped to $|2\rangle$ for optical multi-qubit gates via rotations $\hat{R}(\pi, \phi) = \exp(-i\pi\hat{\sigma}_{12}(\phi)/2)$, with $\hat{\sigma}_{12}(\phi) = \hat{\sigma}_{x12}\cos\phi + \hat{\sigma}_{y12}\sin\phi$, where $\hat{\sigma}_{x12}$ and $\hat{\sigma}_{y12}$ are Pauli matrices for states $|1\rangle$ and $|2\rangle$. The MS interaction $\hat{U}_{02}^{\text{MS}}(\phi)$ between $|0\rangle$ and $|2\rangle$ is expressed exactly as in the main text, with Pauli matrices appropriate to these two levels; defining the global π -rotation on qubits a and b as $\hat{\mathcal{R}}_{12}(\phi) = \hat{R}_{12}(\pi, \phi)_a \otimes \hat{R}_{12}(\pi, \phi)_b$, we find the total unitary $\hat{\mathcal{R}}_{12}(\phi)\hat{U}_{02}^{\text{MS}}(\phi)\hat{\mathcal{R}}_{12}(\phi)$ is independent of the constant laser phase offset ϕ . In fact we note this is not unique to the MS gate and would apply to any optically-implemented unitary.

Such an approach may allow systems to exploit the relatively low power requirements and high addressability of optical interactions, while benefiting from the long memory times and relaxed laser phase stability requirements of microwave qubits.

-
- * Electronic address: mehtak@phys.ethz.ch
- ¹ Leibfried, D., Blatt, R., Monroe, C. & Wineland, D. Quantum dynamics of single trapped ions. *Reviews of Modern Physics* **75**, 281 (2003).
 - ² Häffner, H., Roos, C. F. & Blatt, R. Quantum computing with trapped ions. *Physics Reports* **469**, 155–203 (2008).
 - ³ Monroe, C. & Kim, J. Scaling the ion trap quantum processor. *Science* **339**, 1164–1169 (2013).
 - ⁴ Mehta, K. K. *et al.* Integrated optical addressing of an ion qubit. *Nature Nanotechnology* **11**, 1066 (2016).
 - ⁵ Kielpinski, D., Monroe, C. & Wineland, D. J. Architecture for a large-scale ion-trap quantum computer. *Nature* **417**, 709–711 (2002).
 - ⁶ Keller, J. *et al.* Controlling systematic frequency uncertainties at the 10- 19 level in linear coulomb crystals. *Physical Review A* **99**, 013405 (2019).
 - ⁷ Harty, T. *et al.* High-fidelity preparation, gates, memory, and readout of a trapped-ion quantum bit. *Physical Review Letters* **113**, 220501 (2014).
 - ⁸ Ballance, C., Harty, T., Linke, N., Sepiol, M. & Lucas, D. High-fidelity quantum logic gates using trapped-ion hyperfine qubits. *Physical Review Letters* **117**, 060504 (2016).
 - ⁹ Gaebler, J. P. *et al.* High-fidelity universal gate set for $^9\text{Be}^+$ ion qubits. *Physical Review Letters* **117**, 060505 (2016).
 - ¹⁰ Fowler, A. G., Whiteside, A. C. & Hollenberg, L. C. Towards practical classical processing for the surface code. *Physical Review Letters* **108**, 180501 (2012).
 - ¹¹ Amini, J. M. *et al.* Toward scalable ion traps for quantum information processing. *New Journal of Physics* **12**, 033031 (2010).
 - ¹² Mehta, K. K. & Ram, R. J. Precise and diffraction-limited waveguide-to-free-space focusing gratings. *Scientific Reports* **7**, 2019 (2017).
 - ¹³ Mehta, K. K., Zhang, C., Miller, S. & Home, J. P. Towards fast and scalable trapped-ion quantum logic with integrated photonics. In *Advances in Photonics of Quantum Computing, Memory, and Communication XII*, vol. 10933, 109330B (International Society for Optics and Photonics, 2019).
 - ¹⁴ Wörhoff, K., Heideman, R. G., Leinse, A. & Hoekman, M. TriPleX: a versatile dielectric photonic platform. *Advanced Optical Technologies* **4**, 189–207 (2015).
 - ¹⁵ Chiaverini, J. *et al.* Surface-electrode architecture for ion-trap quantum information processing. *Quantum Information & Computation* **5**, 419–439 (2005).
 - ¹⁶ Mehta, K. *et al.* Ion traps fabricated in a CMOS foundry. *Applied Physics Letters* **105**, 044103 (2014).
 - ¹⁷ Schindler, P. *et al.* A quantum information processor with trapped ions. *New Journal of Physics* **15**, 123012 (2013).
 - ¹⁸ Roos, C. *et al.* Experimental demonstration of ground state laser cooling with electromagnetically induced transparency. *Physical Review Letters* **85**, 5547 (2000).
 - ¹⁹ James, D. F. Quantum dynamics of cold trapped ions with application to quantum computation. *Applied Physics B: Lasers and Optics* **66**, 181–190 (1998).

- ²⁰ Wineland, D. J. *et al.* Experimental issues in coherent quantum-state manipulation of trapped atomic ions. *Journal of Research of the National Institute of Standards and Technology* **103**, 259 (1998).
- ²¹ Brownnutt, M., Kumph, M., Rabl, P. & Blatt, R. Ion-trap measurements of electric-field noise near surfaces. *Reviews of Modern Physics* **87**, 1419 (2015).
- ²² Sørensen, A. & Mølmer, K. Entanglement and quantum computation with ions in thermal motion. *Physical Review A* **62**, 022311 (2000).
- ²³ Leibfried, D. *et al.* Experimental demonstration of a robust, high-fidelity geometric two ion-qubit phase gate. *Nature* **422**, 412 (2003).
- ²⁴ Sedlacek, J. *et al.* Distance scaling of electric-field noise in a surface-electrode ion trap. *Physical Review A* **97**, 020302 (2018).
- ²⁵ Niffenegger, R. J. *et al.* Integrated optical control and enhanced coherence of ion qubits via multi-wavelength photonics. *arXiv preprint arXiv:2001.05052* (2020).
- ²⁶ Milne, A. R. *et al.* Phase-modulated entangling gates robust against static and time-varying errors. *arXiv preprint arXiv:1808.10462* (2018).
- ²⁷ Ma, L.-S., Jungner, P., Ye, J. & Hall, J. L. Delivering the same optical frequency at two places: accurate cancellation of phase noise introduced by an optical fiber or other time-varying path. *Optics letters* **19**, 1777–1779 (1994).
- ²⁸ Srinivas, R. *et al.* Trapped-ion spin-motion coupling with microwaves and a near-motional oscillating magnetic field gradient. *Physical Review Letters* **122**, 163201 (2019).
- ²⁹ Harty, T. *et al.* High-fidelity trapped-ion quantum logic using near-field microwaves. *Physical Review Letters* **117**, 140501 (2016).
- ³⁰ Zanonello, G. *et al.* Robust and resource-efficient microwave near-field entangling $^9\text{Be}^+$ gate. *Physical Review Letters* **123**, 260503 (2019).
- ³¹ Debnath, S. *et al.* Demonstration of a small programmable quantum computer with atomic qubits. *Nature* **536**, 63 (2016).
- ³² Lindenfelser, F., Marinelli, M., Negnevitsky, V., Ragg, S. & Home, J. P. Cooling atomic ions with visible and infrared light. *New Journal of Physics* **19**, 063041 (2017).
- ³³ West, G. N. *et al.* Low-loss integrated photonics for the blue and ultraviolet regime. *APL Photonics* **4**, 026101 (2019).
- ³⁴ Kaufmann, H. *et al.* Scalable creation of long-lived multipartite entanglement. *Physical Review Letters* **119**, 150503 (2017).
- ³⁵ Schäfer, V. *et al.* Fast quantum logic gates with trapped-ion qubits. *Nature* **555**, 75 (2018).
- ³⁶ Saffman, M., Walker, T. G. & Mølmer, K. Quantum information with rydberg atoms. *Reviews of Modern Physics* **82**, 2313 (2010).
- ³⁷ McKenna, T. P. *et al.* Cryogenic packaging of an optomechanical crystal. *Optics Express* **27**, 28782–28791 (2019).
- ³⁸ Leupold, F. M. *Bang-bang Control of a Trapped-Ion Oscillator*. Ph.D. thesis, ETH Zurich (2015).
- ³⁹ Lucas, D. *et al.* Isotope-selective photoionization for calcium ion trapping. *Physical Review A* **69**, 012711 (2004).
- ⁴⁰ Allcock, D. *et al.* Implementation of a symmetric surface-electrode ion trap with field compensation using a modulated raman effect. *New Journal of Physics* **12**, 053026 (2010).
- ⁴¹ Ballance, C. J. *High-fidelity quantum logic in Ca^+* . Ph.D. thesis, Oxford University (2017).
- ⁴² Kotler, S., Akerman, N., Glickman, Y. & Ozeri, R. Nonlinear single-spin spectrum analyzer. *Physical Review Letters* **110**, 110503 (2013).
- ⁴³ Roos, C. *et al.* Nonlinear coupling of continuous variables at the single quantum level. *Physical Review A* **77**, 040302 (2008).
- ⁴⁴ Nie, X. R., Roos, C. F. & James, D. F. Theory of cross phase modulation for the vibrational modes of trapped ions. *Physics Letters A* **373**, 422–425 (2009).
- ⁴⁵ Lechner, R. *et al.* Electromagnetically-induced-transparency ground-state cooling of long ion strings. *Physical Review A* **93**, 053401 (2016).

Acknowledgements

We thank Denys Marchenko, Douwe Geuzebroek, and Arne Leinse at LioniX International for fabrication of the devices and for discussions during design. We are grateful to Vlad Negnevitsky and Matteo Marinelli for their work on the experimental control system and software used for these experiments, and Stefanie Miller for assistance in characterization of fabricated photonic devices. We thank Frank Gürkaynak at ETH for support with CAD software, the ETH FIRST cleanroom staff, and Esther Schlatter for helpful advice on epoxies.

We acknowledge funding from the Swiss National Fund grant no. 200020165555, NCCR QSIT, ETH Zürich, the EU Quantum Flagship, and an ETH Postdoctoral Fellowship.

Author contributions

KKM conceived the work, and designed, characterized, and assembled the trap devices. KKM, CZ, and MM performed the trapped-ion experiments in an apparatus with significant contributions from CZ, MM, TLN, and MS. KKM analyzed the data. JPH supervised the work, and KKM wrote the manuscript with input from all authors.

Additional information

The authors declare no competing financial interests. Correspondences and requests for materials should be addressed to mehtak@phys.ethz.ch.